

Characterizing Mars' magnetotail topology with respect to the upstream interplanetary magnetic fields

Shaosui Xu¹, David L. Mitchell², Tristan Weber³, David Andrew Brain⁴, Janet G Luhmann², Chuanfei Dong⁵, Shannon M. Curry⁶, Ying Juan Ma⁷, Gina A. DiBraccio⁸, Jasper S. Halekas⁹, Yaxue Dong⁴, and Christian Xavier Mazelle¹⁰

¹Space Sciences Lab, UC Berkeley

²University of California, Berkeley

³Laboratory for Atmospheric and Space Physics (LASP)

⁴University of Colorado Boulder

⁵Princeton University

⁶UC Berkeley

⁷University of California Los Angeles

⁸NASA GSFC

⁹University of Iowa

¹⁰IRAP; Université de Toulouse; CNRS; CNES; UPS-OMP; Toulouse, France

November 23, 2022

Abstract

The canonical picture of the magnetotail of unmagnetized planets consists of draped interplanetary magnetic fields (IMF) forming opposite-directed lobes, separated by the current sheet. (missing citation) showed that Mars' magnetotail has a twist departing from this picture. Magnetohydrodynamic (MHD) results suggest that open field lines connected to the planet that populate portions of the tail cause the apparent twist. To validate this interpretation, we compare the tail topology determined from MHD simulations to that inferred from data collected by the Mars Atmosphere and Volatile Evolution (MAVEN) spacecraft, in particular how each topology responds to the upstream IMF orientation. The occurrence rates for open topology from both data and MHD varies with IMF polarities in a similar fashion as the tail twisting. This suggests that Mars' crustal fields have a global effect on the magnetosphere configuration, supporting the picture of a "hybrid" magnetotail that is partly induced/draped and partly intrinsic/planetary in origin.

References

Characterizing Mars' magnetotail topology with respect to the upstream interplanetary magnetic fields

Shaosui Xu¹, David L. Mitchell¹, Tristan Weber², David A. Brain², Janet G. Luhmann¹,
Chuanfei Dong³, Shannon M. Curry¹, Yingjuan Ma⁴, Gina A. DiBraccio⁵, Jasper Halekas⁶,
Yaxue Dong², Christian Mazelle⁷

¹Space Sciences Laboratory, University of California, Berkeley, CA, USA

²Laboratory for Atmospheric and Space Physics, University of Colorado, Boulder, CO, USA

³Department of Astrophysical Sciences and Princeton Plasma Physics Laboratory, Princeton University, Princeton, NJ,
USA

⁴Department of Earth and Space Sciences, University of California, Los Angeles, CA, USA

⁵NASA Goddard Space Flight Center, Greenbelt, MD, USA

⁶Department of Physics and Astronomy, University of Iowa, Iowa City, IA, USA

⁷IRAP, CNRS - University of Toulouse - UPS - CNES, Toulouse, France

Key Points:

- This study provides a detailed mapping of tail magnetic topology at Mars, which is dominated by draped and open magnetic field lines
- Both the MHD model and data show significant changes in Martian tail topology with respect to east/west IMFs
- It implies that Mars' crustal fields have a global effect on the magnetosphere configuration, supporting the picture of a hybrid magnetotail

Corresponding author: Shaosui Xu, shaosui.xu@ssl.berkeley.edu

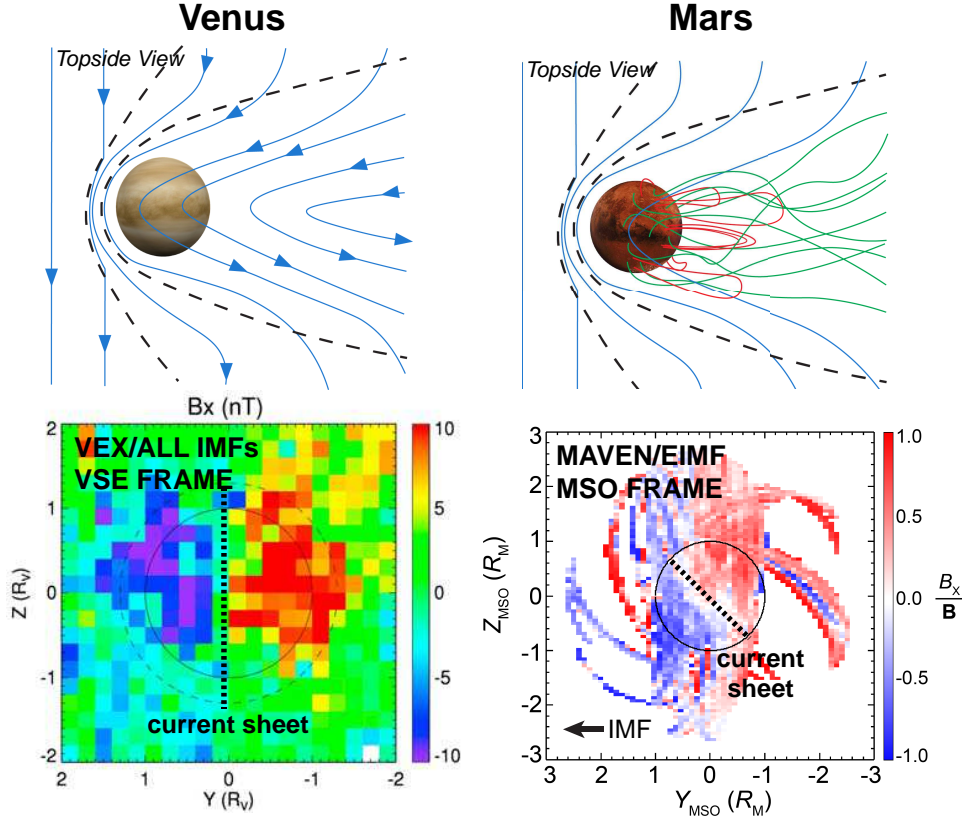
Abstract

The canonical picture of the magnetotail of unmagnetized planets consists of draped interplanetary magnetic fields (IMF) forming opposite-directed lobes, separated by the current sheet. *DiBraccio et al.* [2018] showed that Mars' magnetotail has a twist departing from this picture. Magnetohydrodynamic (MHD) results suggest that open field lines connected to the planet that populate portions of the tail cause the apparent twist. To validate this interpretation, we compare the tail topology determined from MHD simulations to that inferred from data collected by the Mars Atmosphere and Volatile Evolution (MAVEN) spacecraft, in particular how each topology responds to the upstream IMF orientation. The occurrence rates for open topology from both data and MHD varies with IMF polarities in a similar fashion as the tail twisting. This suggests that Mars' crustal fields have a global effect on the magnetosphere configuration, supporting the picture of a "hybrid" magnetotail that is partly induced/draped and partly intrinsic/planetary in origin.

1 Introduction

Venus and Mars both lack an intrinsic global dipole magnetic field but have a significant ionosphere mainly produced by solar extreme ultraviolet photons ionizing the neutral atmosphere, and thus share many similarities in terms of their interaction with the solar wind. Both have an induced magnetosphere formed with the upstream IMF being piled up and draped around the planet. A prominent difference between these two planets is that Mars possesses localized strong crustal magnetic fields [e.g. *Acuna et al.*, 1999; *Connerney et al.*, 2005] that contribute to and modify its induced magnetosphere features on a global scale [e.g. *Brain et al.*, 2007] while Venus has a negligible intrinsic dipole magnetic field at the current epoch [e.g. *Phillips and Russell*, 1987]. As a result, Venus' induced magnetotail consists of two magnetic lobes with oppositely directed magnetic fields formed by draped IMF, separated by a current sheet perpendicular to the plane of the IMF and the solar wind flow [e.g. *Saunders and Russell*, 1986; *Luhmann*, 1986; *McComas et al.*, 1986; *Zhang et al.*, 2010], as illustrated in the left column of Figure 1.

In contrast, Mars' magnetotail departs from this canonical induced-tail picture, having an apparent inter-lobe current sheet twist away from the expected $\pm \mathbf{E}_{\text{conv}}$ location, as reported by *DiBraccio et al.* [2018], also shown in the right column of Figure 1. This twist also varies depending on the IMF sector (hereafter referred as east and west, corresponding to Parker spiral fields pointing away from and toward the sun, as well as $B_y > 0$



48 **Figure 1.** The comparison of the Venus' (the left column) and Mars' magnetotails (the right column). The
 49 top two panels are schematics of the tail configuration and magnetic topologies and the bottom two panels
 50 are the averaged B_x in the tail from measurements by Venus Express and MAVEN, (adopted from Figure 2
 51 of Zhang *et al.* [2010] and Figure 2 of DiBraccio *et al.* [2018]), respectively. The dotted black lines in the
 52 bottom panels indicate the current sheet that separates the two lobes. The lower left panel is for all IMF direc-
 53 tions under the Venus Solar Electric coordinates (VSE) such that the X-axis is antiparallel to the solar wind
 54 flow, the Z-axis aligned with the convection electric field ($\mathbf{E}_{\text{conv}} = -\mathbf{V} \times \mathbf{B}$), and the Y-axis completing the
 55 right-handed system. The lower right panel is in the Mars-centered Solar Orbital (MSO) frame for east IMFs
 56 only. In the MSO frame, the X axis points from the center of Mars to the Sun, the Z axis points to the north
 57 pole of Mars' elliptical orbit plane, and the Y axis completes the right-handed system.

63 and $B_y < 0$, respectively), suggesting Mars' crustal magnetic fields play a role. DiBrac-
 64 cio *et al.* [2018] further compared the tail configuration from MHD with or without crustal
 65 magnetic fields included and revealed that the tail twist was indeed attributed to the in-
 66 clusion of crustal magnetic fields. They proposed that Mars' magnetotail is part of a hy-
 67 brid magnetosphere, consisting of a global intrinsic dipole field (from the low-order dipole

68 term of the crustal magnetism) contribution surrounded by induced/draped fields [*Dubinin*
69 *et al.*, 1980, 1994].

70 Mars' crustal magnetic fields can magnetically reconnect with the IMF [e.g. *Harada*
71 *et al.*, 2017, 2018], giving rise to complex and dynamic magnetic topologies [e.g. *Brain*
72 *et al.*, 2007; *Lillis and Brain*, 2013; *Xu et al.*, 2018a, 2019a; *Weber et al.*, 2019]. Magnetic
73 topology consists of closed (both of the footpoints of a magnetic field line connected to
74 the planet), open (one footpoint of a field line connected to the planet and the other to the
75 solar wind), and draped (both of the footpoints of a field line connected back to the so-
76 lar wind). Mars' magnetotail consists of various magnetic topologies, instead of simply
77 draped like Venus, as reported by previous studies. Nightside tail topology at low altitudes
78 has been studied in detail with Mars Global Surveyor (MGS) data [*Brain et al.*, 2007] and
79 MAVEN data [*Weber et al.*, 2017]. Photoelectrons have been observed in the tail by both
80 the Mars Express (MEx) spacecraft [*Frahm et al.*, 2006, 2010; *Coates et al.*, 2011] and
81 MAVEN [*Xu et al.*, 2016a, 2017a,b], interpreted as magnetic connectivity to the dayside
82 ionosphere through open field lines [*Liemohn et al.*, 2006] or closed field lines [*Xu et al.*,
83 2016a, 2017b]. *Luhmann et al.* [2015a] analyzed magnetic topology from MHD simu-
84 lations and found that a significant portion of Mars' magnetotail is populated with open
85 field lines.

86 The magnetotail topology is also important for characterizing electron precipita-
87 tion [e.g. *Fillingim et al.*, 2007; *Němec et al.*, 2010; *Lillis et al.*, 2011; *Shane et al.*, 2016;
88 *Adams et al.*, 2018] and low-energy ion escape [e.g. *Fränz et al.*, 2015; *Dubinin et al.*,
89 2017; *Inui et al.*, 2018]. Solar wind electrons can precipitate along open field lines, and
90 ionospheric photoelectrons along cross-terminator closed field lines onto the (nightside)
91 atmosphere, causing ionization and auroral emission. Meanwhile, low-energy ions can es-
92 cape along open field lines [e.g. *Ergun et al.*, 2015; *Jakosky et al.*, 2018], partly driven by
93 ambipolar electric fields [e.g. *Collinson et al.*, 2015; *Ergun et al.*, 2016; *Xu et al.*, 2018b;
94 *Akbari et al.*, 2019], and on draped field lines, mainly accelerated by the $\mathbf{J} \times \mathbf{B}$ force
95 and/or the convection electric field [e.g. *Fang et al.*, 2008; *Dong et al.*, 2014; *Halekas*
96 *et al.*, 2017a; *Cravens et al.*, 2017]. More general properties of the Martian magnetotail
97 are discussed in several review papers [*Nagy et al.*, 2004; *Bertucci et al.*, 2011; *Dubinin*
98 *and Fraenz*, 2015; *Liemohn and Xu*, 2018].

99 *DiBraccio et al.* [2018] advocated for the key role of the crustal fields in introducing
100 the twist to Mars' magnetotail with MAVEN magnetic field data and modeling efforts. To
101 further validate the picture of a hybrid Martian magnetotail, we compare the actual tail
102 topology determined from the MHD simulations with topology inferred from the MAVEN
103 superthermal electron data, in particular, how each magnetic topology varies with respect
104 to the upstream IMF polarity. The results of this study on the detailed characterization of
105 the tail topology are also important for understanding the energy and particle exchange
106 between Mars' ionosphere and the solar wind.

107 **2 Methodology**

108 To infer magnetic topology from the MAVEN data, we utilize a new technique de-
109 veloped by *Xu et al.* [2019b] that combines superthermal electrons' energy and pitch angle
110 distributions. This technique mainly relies on three basic principals: (1) the presence of
111 photoelectrons in one or both field-aligned directions indicates the magnetic field line has
112 one or both footpoint(s) embedded in the *dayside* ionosphere at the superthermal elec-
113 tron exobase (~ 160 km, [*Xu et al.*, 2016b]); (2) the presence of loss cones in one or both
114 field-aligned directions indicates the magnetic field line has one or both footpoint(s) em-
115 bedded in the collisional atmosphere; (3) the presence of superthermal electron voids indi-
116 cates both footpoints of the magnetic field line are connected to the nightside atmosphere
117 [*Mitchell et al.*, 2001; *Steckiewicz et al.*, 2015]. Magnetic topology is determined based on
118 where each end of the field line is inferred to connect. One caveat of inferring magnetic
119 topology from electrons is that we can only determine field lines' connectivity to the iono-
120 sphere but not to the planet's surface so that deeply draped field lines can be identified as
121 "open" topology. Photoelectrons can be identified automatically with a shape parameter
122 [*Xu et al.*, 2017a], loss cones with a PAD score [*Weber et al.*, 2017], and electron voids by
123 the electron flux level. The detailed description of how to combine all these aspects to in-
124 fer magnetic topology is provided in *Xu et al.* [2019b]. In this study, we analyze magnetic
125 topology from December 2014 to September 2018, based on the superthermal electron
126 measurements by the Solar Wind Electron Analyzer (SWEA) instrument [*Mitchell et al.*,
127 2016] and magnetic field vector measurements by the magnetometer (MAG) instrument
128 [*Connerney et al.*, 2015] onboard MAVEN .

129 When the MAVEN orbit samples the upstream solar wind, we obtain the IMF clock
130 angle, $\tan^{-1}(B_z/B_y)$ in the MSO frame, directly from MAG measurements in that region

[Halekas *et al.*, 2015, 2017b]. Otherwise, we use a proxy based on MAG measurements in the sheath [Dong *et al.*, 2019]. Thus, each pass through the tail has IMF clock angle estimates both before and after. We then assign each inferred magnetic topology within the magnetosphere with an upstream IMF clock angle by interpolating between the inbound and outbound values.

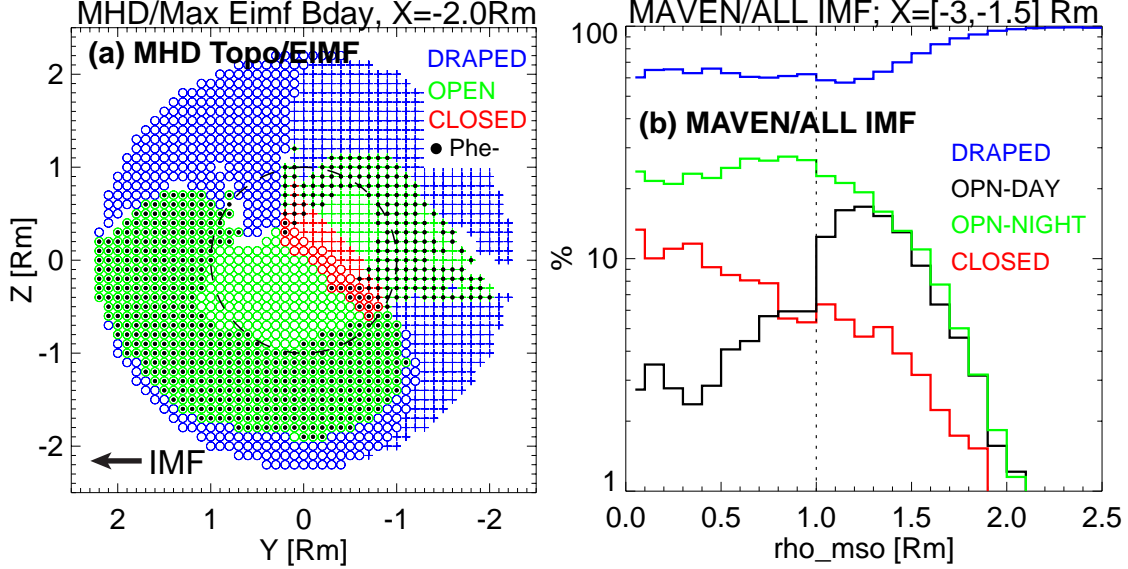
We determine the occurrence rate of the model magnetic topology from 16 steady-state simulations with the multi-species 3-D MHD model [Ma *et al.*, 2002, 2004]. Nominal Parker spiral IMFs and a nominal solar wind proton density (4 cm^{-3}) and speed (400 km/s) with the fall equinox condition are used. Eight simulations are generated for the east IMF ($B_y > 0$) and eight for the west IMF ($B_y < 0$) in the MSO frame. For each IMF direction, the eight simulations consist of the neutral atmospheres and ionization frequencies for the solar maximum and minimum conditions as well as four subsolar longitudes (SSL) for when the southern strong crustal magnetic fields are located on the day-side (SSL = 180°), dawn (SSL = 90°), dusk (SSL = 270°), and nightside (SSL = 0°). For each simulation, magnetic field line tracing starts from a grid of points in the $Y - Z$ plane at $X = -2 R_M$. Magnetic topology for each field line is determined from its connectivity to at 150 km altitude and/or a radial distance of $3 R_M$, where R_M is the Mars radius. The occurrence rate is calculated as the fraction of each magnetic topology type in the respective tail grid for the eight simulations in each IMF sector, i.e. each grid point has eight samples of topology. We note that the models provide steady state “snapshots” of the Mars field topology, which in reality is constantly changing as Mars rotates [Ma *et al.*, 2014].

3 Results

3.1 Data-Model Comparison

As illustrated in the lower right panel of Figure 1, as well as Figure 2 of DiBraccio *et al.* [2018], Mars’ magnetotail has a twist in its lobes and current sheet. MHD results show that this twist also has topological signatures. We take the tail topology from MHD at $X_{MSO} = -2 R_M$ under the east IMF condition as an example, shown in Figure 2a. The tail field topology from MHD consists of draped field lines (blue) in the outmost layer, surrounding mostly open field lines connected to the dayside (green with black dots overplotted), and then open field lines connected to the nightside (green). There is also a

162 central region of closed field lines (red) whose size varies with down-tail distance. This
 163 topology ordering is the same for the other 15 MHD simulations, but varying in exact loca-
 164 tions. A case for the west IMF is shown in Figure S1b in the supplementary material.



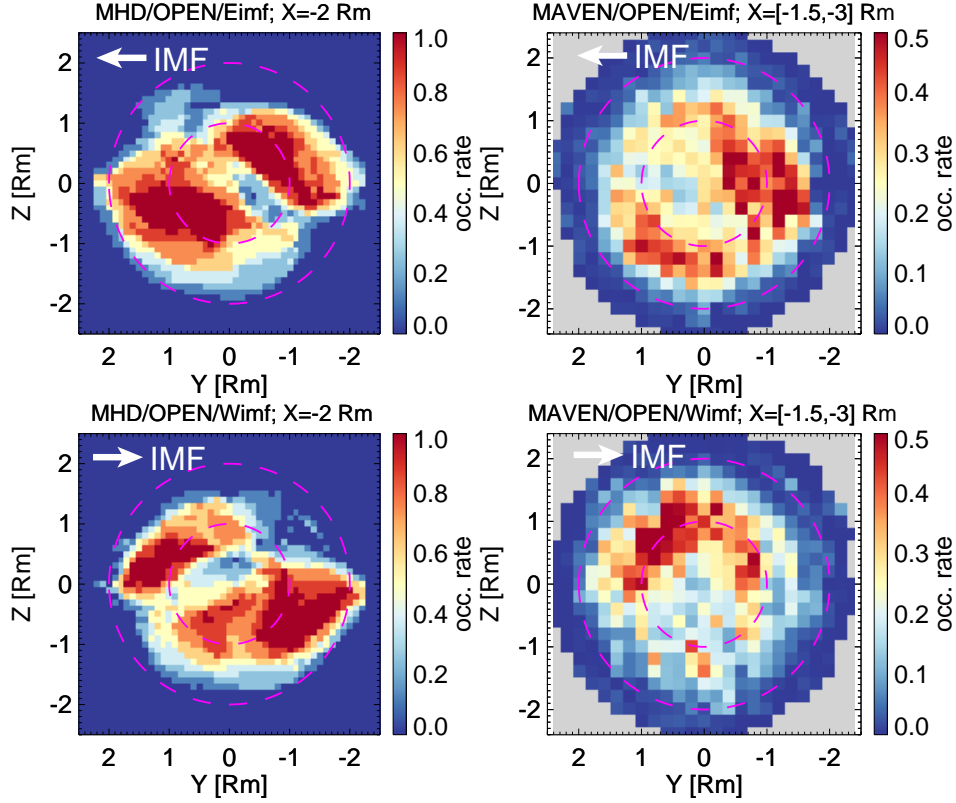
165 **Figure 2.** (a) Magnetic topology from MHD at $X_{MSO} = -2 R_M$ for an east upstream IMF and strong
 166 crustal fields located on the dayside ($SSL=180^\circ$), blue for draped, green for open, and red for closed, with
 167 black dots indicating field lines connected back to dayside. Circles are for $B_x < 0$ and '+' for $B_x > 0$.
 168 (b) The cylindrical averaged occurrence rates of magnetic topologies in the tail ($X_{MSO} = [-1.5, -3] R_M$)
 169 from MAVEN data for all IMFs as a function of $\rho_{MSO} = \sqrt{Y_{MSO}^2 + Z_{MSO}^2}$, blue for draped, black for
 170 open-to-day, green for open-to-night, and red for closed.

171 The magnetic topology inferred from MAVEN data shows a similar ordering, in
 172 the sense of the dominant spatial location for each topology. Figure 2b shows the cylin-
 173 drically averaged occurrence rates of magnetic topologies for all IMFs against $\rho_{MSO} =$
 174 $\sqrt{Y_{MSO}^2 + Z_{MSO}^2}$. We take a cylindrical averaging because the occurrence rates are roughly
 175 cylindrical symmetric (as shown in Figures S1c-S1f in the supplementary material). The
 176 data results show that draped fields occur over 80% of the time for $\rho > 1.5 R_M$, open-to-
 177 day fields are mostly concentrated at $1 < \rho < 1.5 R_M$, open-to-night fields occur most
 178 frequently within the optical shadow, and the occurrence rates for closed fields peak at
 179 10% at the center. This ordering of where each topology occurs most frequently agree
 180 with MHD results.

181 To examine how the IMF polarity affects the tail topology for both MHD and the
 182 data, we compare occurrence rates for the east and west IMF separately. The occurrence
 183 rates from the data have been averaged over all planetary rotations, and over a range of
 184 EUV flux and solar wind conditions. To better capture the twist, we limit our analysis to
 185 data with an upstream IMF clock angle less than 30° or greater than 150° so that the IMF
 186 is mostly in the $X_{MSO} - Y_{MSO}$ plane. In addition, we rotate the frame such that the Y-axis
 187 is parallel or antiparallel to the Y component of the upstream IMF for east and west IMF
 188 sectors, respectively, with X still pointing at the Sun and Z completing the right-handed
 189 system. To approximate this with the MHD simulations, we average the topology in two
 190 groups of eight models ($4 \text{ SSLs} \times 2 \text{ solar conditions}$ for east and west IMF separately).
 191 The comparison is shown in Figure 3. The color range is 0 to 1 for MHD results (left col-
 192 umn) but 0 to 0.5 for MAVEN results (right column), as the occurrence rates from MHD
 193 are roughly twice that of MAVEN data. We use different color ranges to highlight relative
 194 variations in the occurrence rates. Because the sampling of the model averages is different
 195 from the sampling of the data, and because of some limitations of the MHD model (dis-
 196 cussed later), we do not expect detailed agreement. Instead, we use the models to guide
 197 our interpretation.

198 Although the overall occurrence rates from the model and data differ significantly,
 199 the patterns of the occurrence rates and their variation with respect to IMF polarities share
 200 similarities. For east IMF (the top row), the open topology occurs most frequently in the
 201 $+Z/-Y$ and $-Z/+Y$ quadrants in both simulations and data, in agreement with the orienta-
 202 tion of the current sheet for this IMF direction as shown in Figure 2 of *DiBraccio et al.*
 203 [2018]. Some differences between the model and data are expected since the model is
 204 from a thin slice at $X = -2 R_M$ whereas the data are averaged over slice with a thick-
 205 ness of $1.5 R_M$. For west IMF (bottom row), open topology occurs most frequently in
 206 the $+Z/+Y$ quadrant in both simulations and data but only simulations show a significant
 207 region of open topology in the $-Z/-Y$ quadrant. Again, these topological results are in
 208 agreement with a $\sim 90^\circ$ rotation of the current sheet about the X axis when the IMF po-
 209 larity changes from east to west *DiBraccio et al.* [2018].

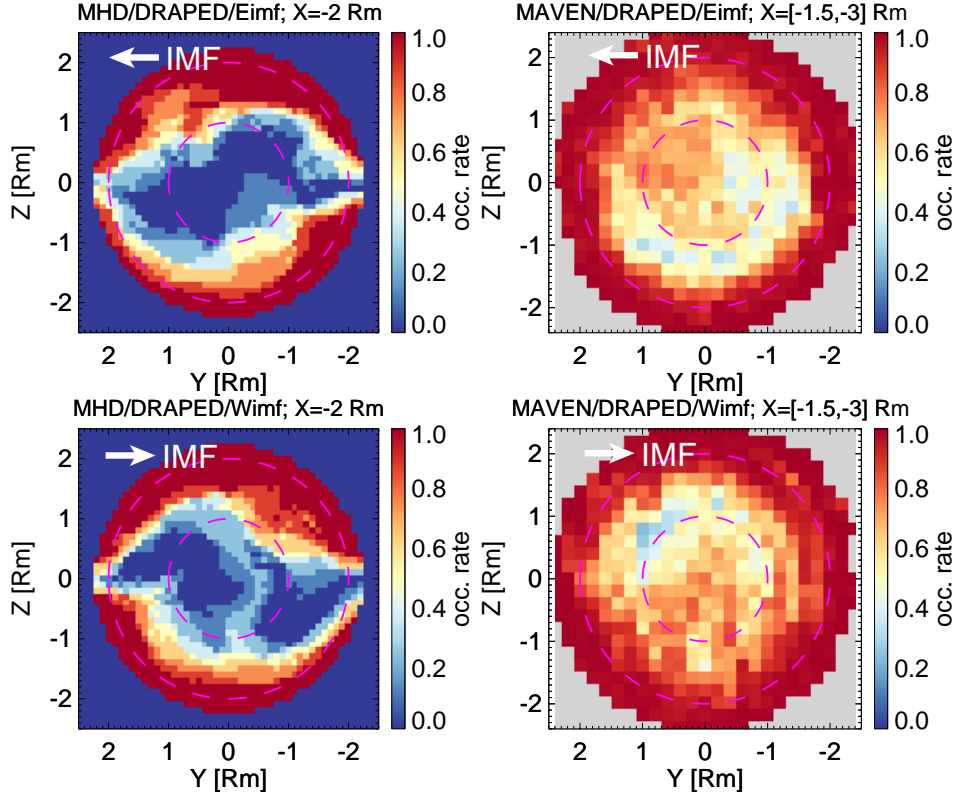
215 The occurrence rates for draped topology from MHD and data are shown in Fig-
 216 ure 4, separated for east and west upstream IMFs. The occurrence rate for draped topol-
 217 ogy in the data is mostly above 50% whereas the open topology shown in Figure 3 has an
 218 occurrence rate below 50%. In contrast, the probability for draped topology from MHD



210 **Figure 3.** Model-data comparison for open topology for east (top row) and west IMF (bottom row). The
 211 left column shows the occurrence rates from MHD at $X_{MSO} = -2 R_M$, calculated from eight simulations
 212 (four SSLs and two solar conditions) separately for each and west IMFs, and right from MAVEN data for
 213 $X_{MSO} = [-1.5, -3] R_M$. Note that the color ranges for the occurrence rates from MHD (the left column) and
 214 data (the right column) are different to highlight features.

219 reaches down to nearly 0 within the two tail lobes, where open topology prevails instead.
 220 Furthermore, MHD predicts a higher occurrence rate of closed field lines near the current
 221 sheet, which is not present in the data (not shown).

225 In summary, the discrepancies between results from the MAVEN data and MHD
 226 modeling include: (a) a factor of two difference in the maximum occurrence rates for
 227 the open topology, (b) occurrence rates in the $-Y/-Z$ quadrant and (c) occurrence rates
 228 for closed field lines. We can identify three possible causes for these differences. First,
 229 the multi-species MHD model relies on numerical diffusion, as a substitute for magnetic
 230 diffusion, to enable magnetic reconnection. It is not known how well this approach ap-
 231 proximates the actual rate of magnetic reconnection. An artificially high reconnection rate



222 **Figure 4.** Model-data comparison for draped topology for east (top row) and west IMF (bottom row). The
 223 same format as Figure 3 but for draped topology. The left column shows the occurrence rates from MHD at
 224 $X_{MSO} = -2 R_M$ and right from MAVEN data $X_{MSO} = [-1.5, -3] R_M$.

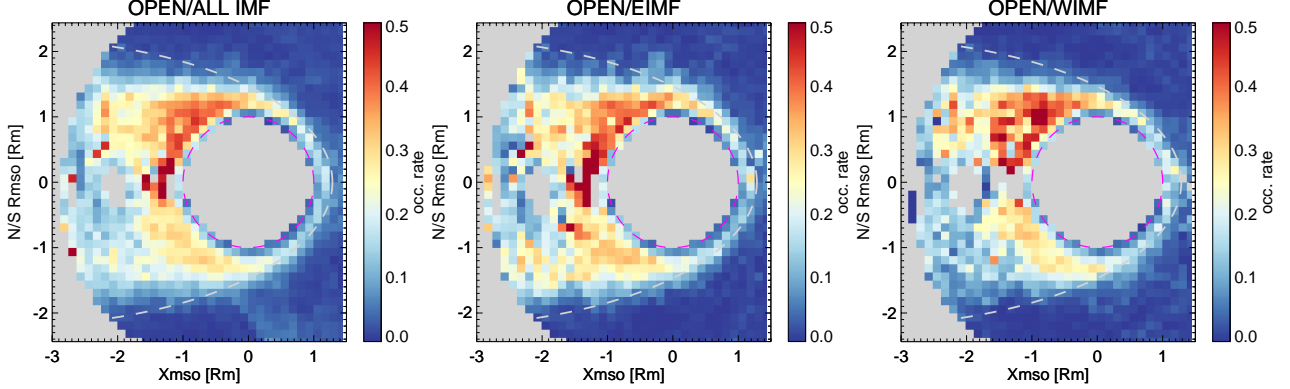
232 would result in more open/closed field lines. Second, the occurrence rate from MHD is
 233 calculated based on only eight steady-state simulations for each IMF polarity, which might
 234 not accurately reflect the actual sampling of data over different seasons and continuously
 235 rotating crustal field orientations. Third, SWEA has an angular resolution of $\sim 20^\circ$, which
 236 might be insufficient to resolve small loss/source cones, expected to be smaller than $< 10^\circ$
 237 over strongly magnetized regions of the crust. This might result in an underestimation of
 238 open field lines associated with strong crustal fields in the south.

239 3.2 Open Topology in the Tail

240 The results above suggest that the presence of a high occurrence rate of open topol-
 241 ogy significantly impacts the Martian magnetotail configuration. It also has important im-
 242 plications for characterizing cold ion outflow and electron precipitation. In Figure 5, we

243 show the occurrence rates for the open topology in the $X_{MSO} - R_{MSO}$ projection, where

$$244 \quad R_{MSO} = \frac{Z_{MSO}}{|Z_{MSO}|} \sqrt{Y_{MSO}^2 + Z_{MSO}^2}.$$



245 **Figure 5.** Occurrence rates of open topology in the $X_{MSO} - R_{MSO}$ projection for all MAVEN data
 246 (left), east (middle), and west IMF (right), respectively. The white dashed lines are conic fits of the induced
 247 magnetic boundary from *Vignes et al.* [2000].

248 Overall, the occurrence rate of the open topology mostly ranges from 20% to 50%
 249 on the nightside, decreasing further down the tail. There is a north-south asymmetry in
 250 Figure 5, with a higher occurrence rate in the north, regardless of the upstream IMF polar-
 251 ity, as the twist in the tail topology is averaged out for each hemisphere. This north-south
 252 asymmetry probably occurs because: (1) cusps of open field lines consist of a small spa-
 253 tial area/solid angle over the southern strong crustal fields; (2) more deeply draped field
 254 lines (into the collisional atmosphere) in the north hemisphere identified as open field
 255 lines by our technique; and (3) we underestimate the occurrence rate over strong crustal
 256 fields due to SWEA's angular resolution. One noticeable difference is that the occurrence
 257 rate for $R_{MSO} < 0$ and $X < -1.5 R_M$ is higher for east IMFs (middle) than west IMFs
 258 (right). Two possible explanations are: (1) the strong crustal fields in the south magne-
 259 tically reconnect more with the east IMF; (2) the solar wind flow in the tail has a compo-
 260 nent preferentially in the opposite direction from the convection electric field, to conserve
 261 momentum after picking up planetary ions, and might push magnetic field lines towards
 262 $-\mathbf{E}_{conv}$, which is $-Z_{MSO}$ for east IMFs but $+Z_{MSO}$ for west IMFs, an effect suggested by
 263 *Chai et al.* [2019].

4 Discussion and Conclusions

Motivated by the evidence that the apparent twist of the Martian magnetotail is caused by reconnection between the IMF and the crustal fields [DiBraccio *et al.*, 2018], we compare magnetic topology inferred from the MAVEN data with that from MHD simulations. From both the model and data, Mars' magnetotail is found to be dominated by combinations of draped and open magnetic topologies, and not merely draped IMFs as at Venus. In addition, the pattern of open field lines in the tail at $X \sim -2 R_M$ downstream varies significantly with the dominant IMF sectors in both data and simulations, in agreement with the tail polarity pattern (e.g. cross-tail current sheet) twisting in opposite directions in response to the different IMFs. These results are consistent with the interpretation that the large portion of open field lines populating the tail produces the twist.

One might argue that magnetic topology inferred from superthermal electrons cannot distinguish deeply draped IMF below the electron exobase from field lines connected to the surface, so that some field lines identified as open by our technique may in fact be deeply draped. However, the variation in occurrence rates of open field lines in response to changes in the IMF polarity supports the interpretation that Mars' crustal magnetic fields cause the tail twist, because the conditions for magnetic reconnection between IMF and crustal magnetic fields depend on IMF polarity. These same conditions also affect where the draped IMF can penetrate deeply into the ionosphere.

This tail topology variation with the IMF polarity also echoes draped field distortions revealed by *Brain et al.* [2006] with MGS observations: the magnetic field at 400-km altitude over a northern weak crustal region is more consistent with a draping pattern under the west IMF but more scattered in directions under the east IMF. *Luhmann et al.* [2015b] showed from MHD simulations that this distortion is likely due to different reconnection geometries for different IMF polarities. While the results from *Brain et al.* [2006] are for dayside, open field lines from dayside magnetic reconnection will populate part of the tail lobes, forming at least part of the open-to-day topology seen in the tail. In all, previous studies and our results suggest that the Martian crustal magnetic fields have a global effect on the magnetosphere configuration, supporting the picture of a hybrid magnetotail at Mars.

294 **Acknowledgments**

295 The MAVEN project is supported by NASA through the Mars Exploration Program. The
296 MAVEN data used in this study are available through Planetary Data System (<https://pds-ppi.igpp.ucla.edu/mission/MAVEN>). The BATS-R-US code is publicly available from
297 <http://csem.engin.umich.edu/tools/swmf>. S. Xu gratefully acknowledges the artistic skills
298 of Jessica Still and the time she dedicated to create the schematics presented in Figure 1.
299

References

- Acuna, M., J. Connerney, R. Lin, D. Mitchell, C. Carlson, J. McFadden, K. Anderson, H. Rème, C. Mazelle, D. Vignes, et al. (1999), Global distribution of crustal magnetization discovered by the Mars Global Surveyor MAG/ER experiment, *Science*, *284*(5415), 790–793.
- Adams, D., S. Xu, D. L. Mitchell, R. L. Lillis, M. Fillingim, L. Andersson, C. Fowler, J. E. P. Connerney, J. Espley, and C. Mazelle (2018), Using Magnetic Topology to Probe the Sources of Mars' Nightside Ionosphere, *Geophysical Research Letters*, *0*(ja), doi:10.1029/2018GL080629.
- Akbari, H., L. Andersson, W. Peterson, J. Espley, M. Benna, and R. Ergun (2019), Ambipolar Electric Field in the Martian Ionosphere: MAVEN Measurements, *Journal of Geophysical Research: Space Physics*, *124*(6), 4518–4524.
- Bertucci, C., F. Duru, N. Edberg, M. Fraenz, C. Martinecz, K. Szego, and O. Vaisberg (2011), The induced magnetospheres of mars, venus, and titan, *Space science reviews*, *162*(1-4), 113–171.
- Brain, D., R. Lillis, D. Mitchell, J. Halekas, and R. Lin (2007), Electron pitch angle distributions as indicators of magnetic field topology near Mars, *Journal of Geophysical Research: Space Physics (1978–2012)*, *112*(A9).
- Brain, D. A., D. L. Mitchell, and J. S. Halekas (2006), The magnetic field draping direction at Mars from April 1999 through August 2004, *Icarus*, *182*(2), 464–473.
- Chai, L., W. Wan, Y. Wei, T. Zhang, W. Exner, M. Fraenz, E. Dubinin, M. Feyerabend, U. Motschmann, Y. Ma, et al. (2019), The Induced Global Looping Magnetic Field on Mars, *The Astrophysical Journal Letters*, *871*(2), L27.
- Coates, A. J., S. Tsang, A. Wellbrock, R. Frahm, J. Winningham, S. Barabash, R. Lundin, D. Young, and F. Crary (2011), Ionospheric photoelectrons: Comparing Venus, Earth, Mars and Titan, *Planetary and Space Science*, *59*(10), 1019–1027.
- Collinson, G., D. Mitchell, A. Glocer, J. Grebowsky, W. K. Peterson, J. Connerney, L. Andersson, J. Espley, C. Mazelle, J.-A. Sauvaud, A. Fedorov, Y. Ma, S. Bougher, R. Lillis, R. Ergun, and B. Jakosky (2015), Electric Mars: The first direct measurement of an upper limit for the Martian "polar wind" electric potential, *Geophysical Research Letters*, *42*(21), 9128–9134, doi:10.1002/2015GL065084, 2015GL065084.
- Connerney, J., M. Acuña, N. Ness, G. Kletetschka, D. Mitchell, R. Lin, and H. Reme (2005), Tectonic implications of Mars crustal magnetism, *Proceedings of the national*

- 333 *Academy of Sciences of the United States of America*, 102(42), 14,970–14,975.
- 334 Connerney, J., J. Espley, P. Lawton, S. Murphy, J. Odom, R. Oliverson, and D. Sheppard
335 (2015), The MAVEN magnetic field investigation, *Space Science Reviews*, pp. 1–35.
- 336 Cravens, T. E., O. Hamil, S. Houston, S. Bougher, Y. Ma, D. Brain, and S. Ledvina
337 (2017), Estimates of ionospheric transport and ion loss at mars, *Journal of Geophysical
338 Research: Space Physics*, 122(10), 10,626–10,637, doi:10.1002/2017JA024582.
- 339 DiBraccio, G. A., J. G. Luhmann, S. M. Curry, J. R. Espley, S. Xu, D. L. Mitchell, Y. Ma,
340 C. Dong, J. R. Gruesbeck, J. E. P. Connerney, Y. Harada, S. Ruhunusiri, J. S. Halekas,
341 Y. Soobiah, T. Hara, D. A. Brain, and B. M. Jakosky (2018), The Twisted Configura-
342 tion of the Martian Magnetotail: MAVEN Observations, *Geophysical Research Letters*,
343 45(10), 4559–4568, doi:10.1029/2018GL077251.
- 344 Dong, C., S. W. Bougher, Y. Ma, G. Toth, A. F. Nagy, and D. Najib (2014), Solar wind
345 interaction with Mars upper atmosphere: Results from the one-way coupling between
346 the multifluid MHD model and the MTGCM model, *Geophysical Research Letters*, 41,
347 2708–2715, doi:10.1002/2014GL059515.
- 348 Dong, Y., X. Fang, D. Brain, D. Hurley, J. Halekas, J. Espley, R. Ramstad, S. Ruhunusiri,
349 and B. Jakosky (2019), Magnetic field in the Martian magnetosheath and the application
350 as an IMF clock angle proxy, *Journal of Geophysical Research: Space Physics*.
- 351 Dubinin, E., and M. Fraenz (2015), Magnetotails of mars and venus, in *Magnetotails in
352 the solar system*, vol. 207, pp. 34–59, John Wiley Hoboken, NJ.
- 353 Dubinin, E., R. Lundin, and K. Schwingenschuh (1994), Solar wind electrons as tracers
354 of the martian magnetotail topology, *Journal of Geophysical Research: Space Physics*,
355 99(A11), 21,233–21,240.
- 356 Dubinin, E., M. Fraenz, M. Pätzold, J. McFadden, J. Halekas, G. DiBraccio, J. Connerney,
357 F. Eparvier, D. Brain, B. Jakosky, et al. (2017), The effect of solar wind variations on
358 the escape of oxygen ions from Mars through different channels: MAVEN observations,
359 *Journal of Geophysical Research: Space Physics*, 122(11), 11–285.
- 360 Dubinin, E. M., P. Izrailevich, and I. Podgorny (1980), The combined magnetosphere,
361 *Kosmicheskie Issledovaniia*, 18, 470–474.
- 362 Ergun, R. E., M. W. Morooka, L. A. Andersson, C. M. Fowler, G. T. Delory, D. J.
363 Andrews, A. I. Eriksson, T. McEnulty, and B. M. Jakosky (2015), Dayside elec-
364 tron temperature and density profiles at mars: First results from the maven langmuir
365 probe and waves instrument, *Geophysical Research Letters*, 42(21), 8846–8853, doi:

- 366 10.1002/2015GL065280.
- 367 Ergun, R. E., L. A. Andersson, C. M. Fowler, A. K. Woodson, T. D. Weber, G. T. Delory,
368 D. J. Andrews, A. I. Eriksson, T. McEnulty, M. W. Morooka, A. I. F. Stewart, P. Ma-
369 haffy, and B. M. Jakosky (2016), Enhanced o^{2+} loss at Mars due to an ambipolar elec-
370 tric field from electron heating, *Journal of Geophysical Research: Space Physics*, *121*(5),
371 4668–4678, doi:10.1002/2016JA022349.
- 372 Fang, X., M. W. Liemohn, A. F. Nagy, Y. Ma, D. L. De Zeeuw, J. U. Kozyra, and T. H.
373 Zurbuchen (2008), Pickup oxygen ion velocity space and spatial distribution around
374 Mars, *Journal of Geophysical Research: Space Physics*, *113*(A2).
- 375 Fillingim, M. O., L. M. Peticolas, R. J. Lillis, D. A. Brain, J. S. Halekas, D. L. Mitchell,
376 R. P. Lin, D. Lummerzheim, S. W. Bougher, and D. L. Kirchner (2007), Model calcu-
377 lations of electron precipitation induced ionization patches on the nightside of Mars,
378 *Geophysical Research Letters*, *34*, L12101, doi:10.1029/2007GL029986.
- 379 Frahm, R., J. Sharber, J. Winningham, P. Wurz, M. Liemohn, E. Kallio, M. Yamauchi,
380 R. Lundin, S. Barabash, A. Coates, et al. (2006), Locations of atmospheric photoelec-
381 tron energy peaks within the Mars environment, *Space Science Reviews*, *126*(1-4), 389–
382 402.
- 383 Frahm, R., J. Sharber, J. Winningham, R. Link, M. Liemohn, J. Kozyra, A. Coates,
384 D. Linder, S. Barabash, R. Lundin, et al. (2010), Estimation of the escape of photo-
385 electrons from Mars in 2004 liberated by the ionization of carbon dioxide and atomic
386 oxygen, *Icarus*, *206*(1), 50–63.
- 387 Fränz, M., E. Dubinin, D. Andrews, S. Barabash, H. Nilsson, and A. Fedorov (2015),
388 Cold ion escape from the Martian ionosphere, *Planetary and Space Science*, *119*, 92–
389 102.
- 390 Halekas, J., E. Taylor, G. Dalton, G. Johnson, D. Curtis, J. McFadden, D. Mitchell,
391 R. Lin, and B. Jakosky (2015), The solar wind ion analyzer for MAVEN, *Space Science*
392 *Reviews*, *195*(1-4), 125–151.
- 393 Halekas, J., D. Brain, J. Luhmann, G. DiBraccio, S. Ruhunusiri, Y. Harada, C. Fowler,
394 D. Mitchell, J. Connerney, J. Espley, et al. (2017a), Flows, Fields, and Forces in the
395 Mars-Solar Wind Interaction, *Journal of Geophysical Research: Space Physics*, *122*(11).
- 396 Halekas, J., S. Ruhunusiri, Y. Harada, G. Collinson, D. Mitchell, C. Mazelle, J. McFad-
397 den, J. Connerney, J. Espley, F. Eparvier, et al. (2017b), Structure, dynamics, and sea-
398 sonal variability of the Mars-solar wind interaction: MAVEN Solar Wind Ion Ana-

- 399 lyzer in-flight performance and science results, *Journal of Geophysical Research: Space*
400 *Physics*, 122(1), 547–578.
- 401 Harada, Y., J. Halekas, J. McFadden, J. Espley, G. DiBraccio, D. Mitchell, C. Mazelle,
402 D. Brain, L. Andersson, Y. Ma, et al. (2017), Survey of magnetic reconnection signa-
403 tures in the Martian magnetotail with MAVEN, *Journal of Geophysical Research: Space*
404 *Physics*.
- 405 Harada, Y., J. S. Halekas, G. A. DiBraccio, S. Xu, J. Espley, J. P. Mcfadden, D. L.
406 Mitchell, C. Mazelle, D. A. Brain, T. Hara, Y. J. Ma, S. Ruhunusiri, and B. M.
407 Jakosky (2018), Magnetic Reconnection on Dayside Crustal Magnetic Fields at
408 Mars: MAVEN Observations, *Geophysical Research Letters*, 45(10), 4550–4558, doi:
409 10.1002/2018GL077281.
- 410 Inui, S., K. Seki, S. Sakai, D. Brain, T. Hara, J. McFadden, J. Halekas, D. Mitchell,
411 G. DiBraccio, and B. Jakosky (2018), Statistical Study of Heavy Ion Outflows From
412 Mars Observed in the Martian-Induced Magnetotail by MAVEN, *Journal of Geophysical*
413 *Research: Space Physics*.
- 414 Jakosky, B., D. Brain, M. Chaffin, S. Curry, J. Deighan, J. Grebowsky, J. Halekas,
415 F. Leblanc, R. Lillis, J. Luhmann, et al. (2018), Loss of the Martian atmosphere to
416 space: Present-day loss rates determined from MAVEN observations and integrated loss
417 through time, *Icarus*, 315, 146 – 157, doi:https://doi.org/10.1016/j.icarus.2018.05.030.
- 418 Liemohn, M. W., and S. Xu (2018), Recent advances regarding the mars magnetotail cur-
419 rent sheet, *Electric Currents in Geospace and Beyond*, 235, 177.
- 420 Liemohn, M. W., Y. Ma, R. A. Frahm, X. Fang, J. U. Kozyra, A. F. Nagy, J. D. Winning-
421 ham, J. R. Sharber, S. Barabash, and R. Lundin (2006), Mars Global MHD Predictions
422 of Magnetic Connectivity Between the Dayside Ionosphere and the Magnetospheric
423 Flanks, *Space Science Reviews*, 126, 63–76, doi:10.1007/s11214-006-9116-8.
- 424 Lillis, R. J., and D. A. Brain (2013), Nightside electron precipitation at Mars: Geographic
425 variability and dependence on solar wind conditions, *Journal of Geophysical Research:*
426 *Space Physics*, 118(6), 3546–3556.
- 427 Lillis, R. J., M. O. Fillingim, and D. A. Brain (2011), Three-dimensional structure of
428 the Martian nightside ionosphere: Predicted rates of impact ionization from Mars
429 Global Surveyor magnetometer and electron reflectometer measurements of precipi-
430 tating electrons, *Journal of Geophysical Research (Space Physics)*, 116(A15), A12317,
431 doi:10.1029/2011JA016982.

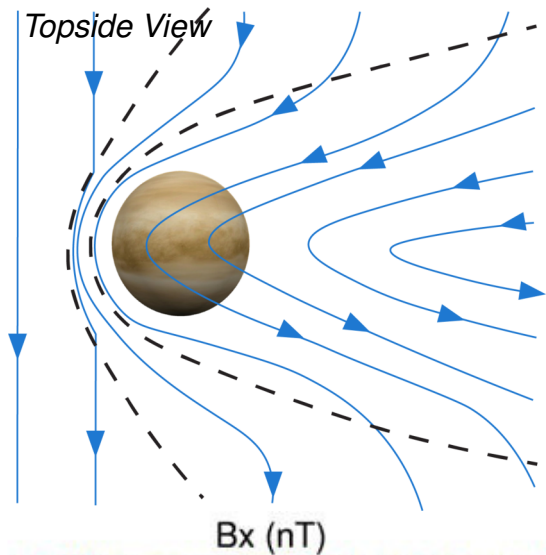
- 432 Luhmann, J. (1986), The solar wind interaction with Venus, *Space science reviews*, 44(3-
433 4), 241–306.
- 434 Luhmann, J., C. Dong, Y. Ma, S. Curry, D. Mitchell, J. Espley, J. Connerney, J. Halekas,
435 D. Brain, B. Jakosky, et al. (2015a), Implications of MAVEN Mars near-wake measure-
436 ments and models, *Geophysical Research Letters*, 42(21), 9087–9094.
- 437 Luhmann, J., Y.-J. Ma, D. Brain, D. Ulusen, R. Lillis, J. Halekas, and J. Espley (2015b),
438 Solar wind interaction effects on the magnetic fields around Mars: Consequences for
439 interplanetary and crustal field measurements, *Planetary and Space Science*, 117, 15–23.
- 440 Ma, Y., A. F. Nagy, K. C. Hansen, D. L. DeZeeuw, T. I. Gombosi, and K. Powell (2002),
441 Three-dimensional multispecies MHD studies of the solar wind interaction with Mars
442 in the presence of crustal fields, *Journal of Geophysical Research: Space Physics* (1978–
443 2012), 107(A10), 1282–1289.
- 444 Ma, Y., A. F. Nagy, I. V. Sokolov, and K. C. Hansen (2004), Three-dimensional, multi-
445 species, high spatial resolution MHD studies of the solar wind interaction with Mars,
446 *Journal of Geophysical Research: Space Physics* (1978–2012), 109(A7).
- 447 Ma, Y., X. Fang, C. T. Russell, A. F. Nagy, G. Toth, J. G. Luhmann, D. A. Brain, and
448 C. Dong (2014), Effects of crustal field rotation on the solar wind plasma interaction
449 with Mars, *Geophysical Research Letters*, 41(19), 6563–6569.
- 450 McComas, D. J., H. E. Spence, C. Russell, and M. Saunders (1986), The average mag-
451 netic field draping and consistent plasma properties of the Venus magnetotail, *Journal*
452 *of Geophysical Research: Space Physics*, 91(A7), 7939–7953.
- 453 Mitchell, D., R. Lin, C. Mazelle, H. Reme, P. Cloutier, J. Connerney, M. Acuña, and
454 N. Ness (2001), Probing Mars' crustal magnetic field and ionosphere with the MGS
455 Electron Reflectometer, *Journal of Geophysical Research: Planets* (1991–2012),
456 106(E10), 23,419–23,427.
- 457 Mitchell, D., C. Mazelle, J.-A. Sauvaud, J.-J. Thocaven, J. Rouzaud, A. Fedorov,
458 P. Rouger, D. Toublanc, E. Taylor, D. Gordon, et al. (2016), The MAVEN solar wind
459 electron analyzer, *Space Science Reviews*, 200(1-4), 495–528.
- 460 Nagy, A., D. Winterhalter, K. Sauer, T. Cravens, S. Brecht, C. Mazelle, D. Crider,
461 E. Kallio, A. Zakharov, E. Dubinin, et al. (2004), The plasma environment of Mars,
462 in *Mars? Magnetism and Its Interaction with the Solar Wind*, pp. 33–114, Springer.
- 463 Němec, F., D. Morgan, D. Gurnett, and F. Duru (2010), Nightside ionosphere of Mars:
464 Radar soundings by the Mars Express spacecraft, *Journal of Geophysical Research:*

- 465 *Planets (1991–2012)*, 115(E12).
- 466 Phillips, J., and C. Russell (1987), Revised upper limit on the internal magnetic moment
467 of Venus, *Advances in space research*, 7(12), 291–294.
- 468 Saunders, M., and C. Russell (1986), Average dimension and magnetic structure of the
469 distant Venus magnetotail, *Journal of Geophysical Research: Space Physics*, 91(A5),
470 5589–5604.
- 471 Shane, A. D., S. Xu, M. W. Liemohn, and D. L. Mitchell (2016), Mars nightside elec-
472 trons over strong crustal fields, *Journal of Geophysical Research: Space Physics*, 121(4),
473 3808–3823.
- 474 Steckiewicz, M., C. Mazelle, P. Garnier, N. Andr. Penou, A. Beth, J.-A. Sauvaud, D. Tou-
475 blanc, D. L. Mitchell, J. P. McFadden, J. G. Luhmann, R. J. Lillis, J. E. P. Connerney,
476 J. R. Espley, L. Andersson, J. S. Halekas, D. E. Larson, and B. M. Jakosky (2015),
477 Altitude dependence of nightside Martian suprathermal electron depletions as re-
478 vealed by MAVEN observations, *Geophysical Research Letters*, pp. 8877–8884, doi:
479 10.1002/2015GL065257, 2015GL065257.
- 480 Vignes, D., C. Mazelle, H. Rme, M. H. Acuña, J. E. P. Connerney, R. P. Lin, D. L.
481 Mitchell, P. Cloutier, D. H. Crider, and N. F. Ness (2000), The solar wind interaction
482 with Mars: Locations and shapes of the bow shock and the magnetic pile-up bound-
483 ary from the observations of the MAG/ER Experiment onboard Mars Global Surveyor,
484 *Geophysical Research Letters*, 27, 49–52, doi:10.1029/1999GL010703.
- 485 Weber, T., D. Brain, D. Mitchell, S. Xu, J. Connerney, and J. Halekas (2017), Characteri-
486 zation of Low-Altitude Nightside Martian Magnetic Topology Using Electron Pitch An-
487 gles Distributions, *Journal of Geophysical Research: Space Physics*, 122(10), 9777–9789,
488 doi:10.1002/2017JA024491, 2017JA024491.
- 489 Weber, T., D. Brain, D. Mitchell, S. Xu, J. Espley, J. Halekas, R. Lillis, and B. Jakosky
490 (2019), The Influence of Solar Wind Pressure on Martian Crustal Magnetic Field Topol-
491 ogy, *Geophysical Research Letters*, 46(5), 2347–2354.
- 492 Xu, S., D. Mitchell, M. Liemohn, C. Dong, S. Bougher, M. Fillingim, R. Lillis, J. McFad-
493 den, C. Mazelle, J. Connerney, and B. Jakosky (2016a), Deep nightside photoelectron
494 observations by MAVEN SWEA: Implications for Martian northern hemispheric mag-
495 netic topology and nightside ionosphere source, *Geophysical Research Letters*, 43(17),
496 8876–8884, doi:10.1002/2016GL070527, 2016GL070527.

- 497 Xu, S., M. Liemohn, S. Bougher, and D. Mitchell (2016b), Martian high-altitude photo-
498 electrons independent of solar zenith angle, *Journal of Geophysical Research: Space*
499 *Physics*, *121*(4), 3767–3780, doi:10.1002/2015JA022149, 2015JA022149.
- 500 Xu, S., D. Mitchell, M. Liemohn, X. Fang, Y. Ma, J. Luhmann, D. Brain, M. Steckiewicz,
501 C. Mazelle, J. Connerney, and B. Jakosky (2017a), Martian low-altitude magnetic topol-
502 ogy deduced from MAVEN/SWEA observations, *Journal of Geophysical Research:*
503 *Space Physics*, *122*(2), 1831–1852, doi:10.1002/2016JA023467, 2016JA023467.
- 504 Xu, S., D. Mitchell, J. Luhmann, Y. Ma, X. Fang, Y. Harada, T. Hara, D. Brain, T. Web-
505 ber, C. Mazelle, and G. A. DiBraccio (2017b), High-altitude closed magnetic loops at
506 Mars observed by MAVEN, *Geophysical Research Letters*, *44*(22), 11,229–11,238, doi:
507 10.1002/2017GL075831, 2017GL075831.
- 508 Xu, S., X. Fang, D. L. Mitchell, Y. Ma, J. G. Luhmann, G. A. DiBraccio, T. Weber,
509 D. Brain, C. Mazelle, S. M. Curry, and C. O. Lee (2018a), Investigation of Martian
510 Magnetic Topology Response to 2017 September ICME, *Geophysical Research Letters*,
511 *45*(15), 7337–7346, doi:10.1029/2018GL077708.
- 512 Xu, S., D. L. Mitchell, J. P. McFadden, G. Collinson, Y. Harada, R. Lillis,
513 C. Mazelle, and J. E. P. Connerney (2018b), Field-aligned potentials at mars from
514 maven observations, *Geophysical Research Letters*, *45*(19), 10,119–10,127, doi:
515 10.1029/2018GL080136.
- 516 Xu, S., S. M. Curry, D. L. Mitchell, J. G. Luhmann, R. J. Lillis, and C. Dong (2019a),
517 Magnetic topology response to the 2003 Halloween ICME event at Mars, *Journal of*
518 *Geophysical Research: Space Physics*, *124*(1), 151–165.
- 519 Xu, S., T. Weber, D. L. Mitchell, D. A. Brain, C. Mazelle, G. A. DiBraccio, and J. Esp-
520 ley (2019b), A technique to infer magnetic topology at Mars and its application to the
521 terminator region, *Journal of Geophysical Research: Space Physics*, *124*(3), 1823–1842.
- 522 Zhang, T., W. Baumjohann, J. Du, R. Nakamura, R. Jarvinen, E. Kallio, A. Du, M. Ba-
523 likhin, J. Luhmann, and C. Russell (2010), Hemispheric asymmetry of the magnetic
524 field wrapping pattern in the Venusian magnetotail, *Geophysical Research Letters*,
525 *37*(14).

Figure 1.

Venus



Mars

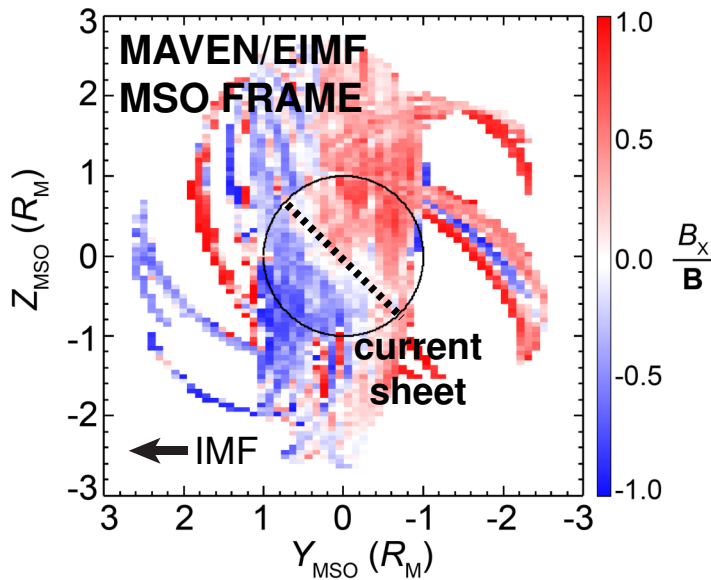
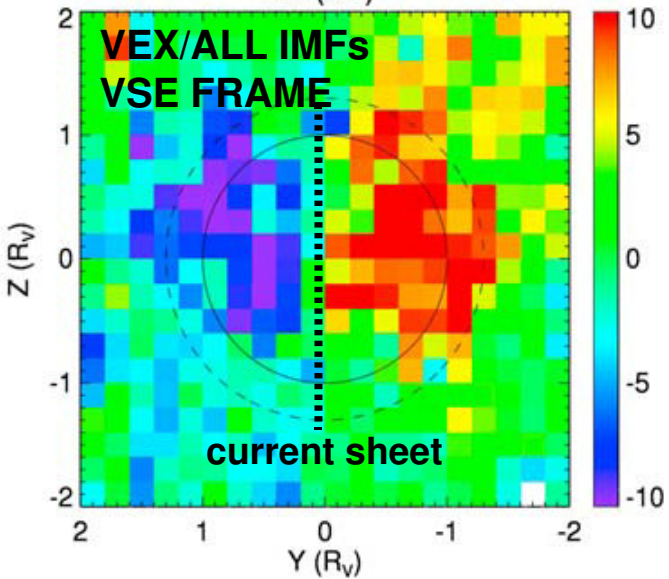
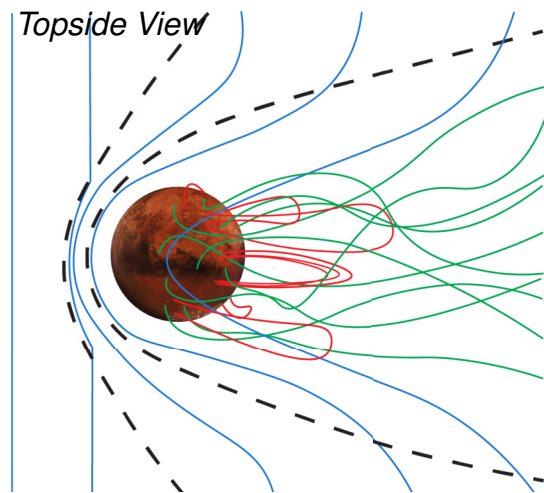
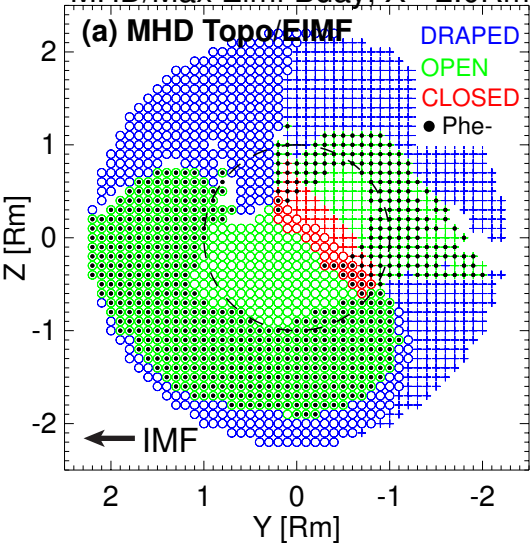


Figure 2.

MHD/Max Eimf Bday, X=-2.0Rm



MAVEN/ALL IMF; X=[-3,-1.5] Rm

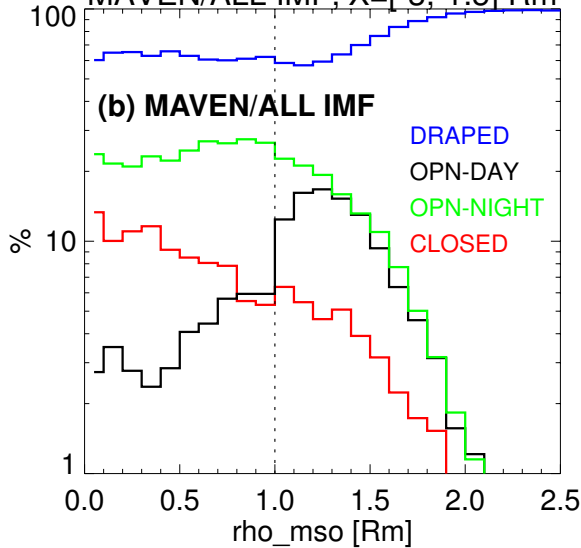
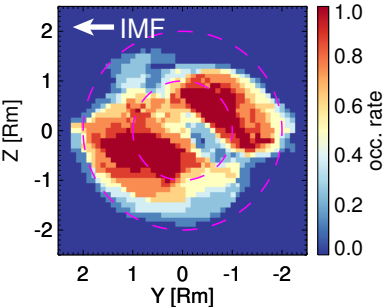
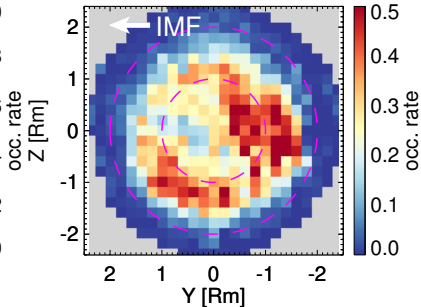


Figure 3.

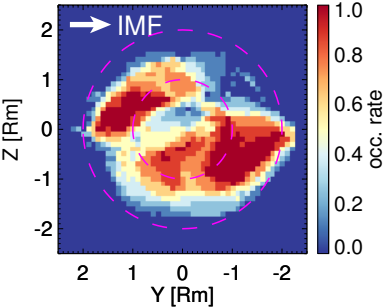
MHD/OPEN/Eimf; X=-2 Rm



MAVEN/OPEN/Eimf; X=[-1.5,-3] Rm



MHD/OPEN/Wimf; X=-2 Rm



MAVEN/OPEN/Wimf; X=[-1.5,-3] Rm

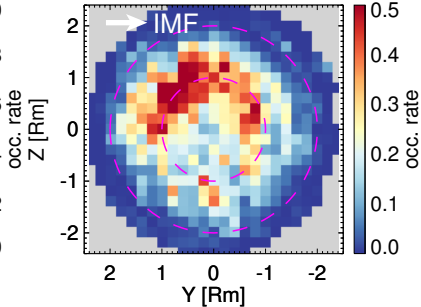
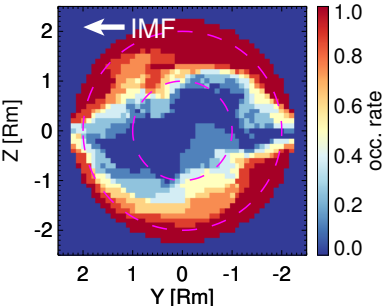
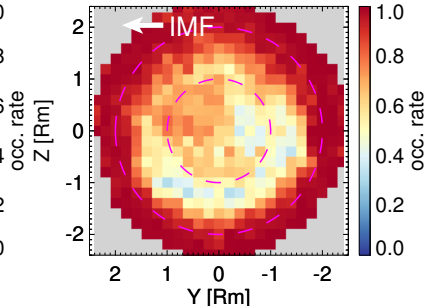


Figure 4.

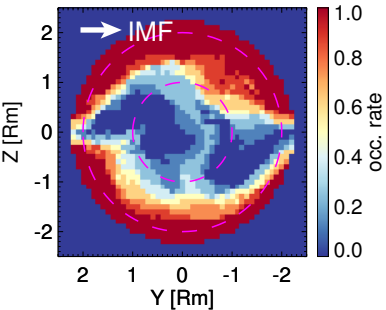
MHD/DRAPED/Eimf; X=-2 Rm



MAVEN/DRAPED/Eimf; X=[-1.5,-3] Rm



MHD/DRAPED/Wimf; X=-2 Rm



MAVEN/DRAPED/Wimf; X=[-1.5,-3] Rm

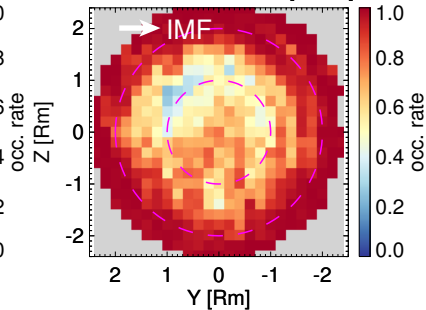
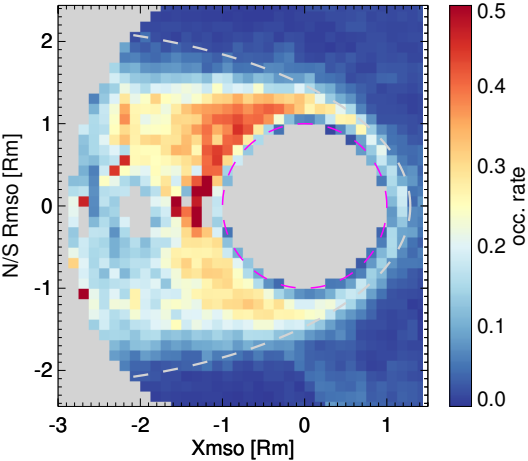
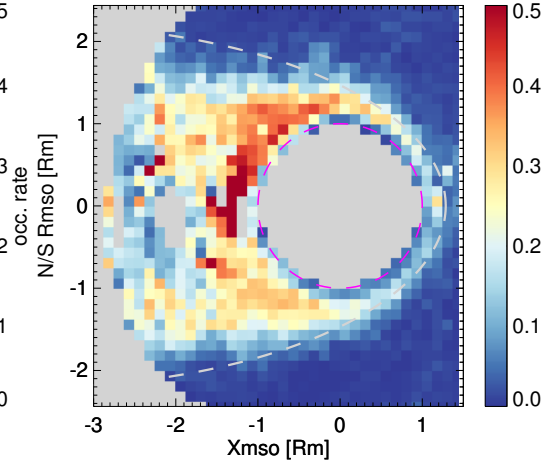


Figure 5.

OPEN/ALL IMF



OPEN/EIMF



OPEN/WIMF

